Geophysical and Astrophysical Fluid Dynamics
Vol. 00, No. 00, 00 Month 20xx, 1–25

Spectra of atmospheric water in precipitating quasi-geostrophic turbulence

Thomas K. Edwards†* , Leslie M. Smith†‡ and Samuel N. Stechmann‡§

† Department of Mathematics, University of Wisconsin,Madison, WI 53706, USA
‡ Department of Engineering Physics, University of Wisconsin,Madison, WI 53706, USA
§Department of Atmospheric and Oceanic Sciences, University of Wisconsin, Madison, WI 53706, USA

(*Submitted June 2019; Revised September 2019*)

Atmospheric water has a complex behavior partly due to the influence of precipitation. Consequently, it is challenging to explain properties of water such as the scale-dependence of its variance, for which a range of spectral exponents has been identified in observational data. Here, a precipitating quasi-geostrophic (PQG) model is explored as a possible prototype for contributing to understanding of water spectra, in an idealized setting. Geostrophic turbulence is examined in numerical simulations, where precipitation is included to explore its effect on the water spectrum, but where phase changes are neglected to allow corresponding theoretical analysis. The water spectral exponent is seen to range from approximately -1.4 to approximately -5 depending on the rainfall speed parameter, V_r, which indicates a significant influence of precipitation on the water spectrum. The limiting values of this range are explained through asymptotic analyses for large and small values of V_r. To obtain this theoretical understanding of the model, a key observation is that water can be written as a linear combination of two other tracers (equivalent potential temperature and a moist variable M), which themselves have theoretically tractable spectra. These two other tracers are linked to distinct modes of the PQG equations—the vortical mode and a moist mode—and the analysis here highlights the usefulness of wave or mode decompositions for understanding water in a saturated domain.

Keywords: Precipitating quasi-geostrophic equations; water spectra; asymptotics

1. Introduction

Atmospheric water is notoriously difficult to model, predict, and understand. This is in part due to the multitude of physical processes involved in the dynamics of water, such as precipitation and related processes.

The power spectrum of water—i.e., the scale dependence of its variance—seems to reflect water's complex physics and dynamics. In particular, a range of spectral exponents has been reported in observations of water, as widely as a range of -1.3 to -2.7 (see, e.g., section 3.1 of Fischer *et al.* 2012), but more commonly in terms of simpler fractions, in part motivated by turbulence theory, as a range of $-5/3$ to -2 (Nastrom *et al.* 1986, Cho *et al.* 2000, Kahn and Teixeira 2009, Kahn *et al.* 2011, Fischer *et al.* 2012, Pressel and Collins 2012). A variety of factors could influence the spectrum of water, such as, e.g., precipitation and meridional and vertical gradients of the background state, and by investigating the influence of different factors, a better understanding of the physics and dynamics of water could be obtained.

In the present paper, the overarching question is: Can some theoretical insight be gained for the spectrum of water, at least in an idealized setup? To carry out the investigation here, a quasi-geostrophic (QG) framework is used. The great advantage of the QG framework is that it is simple enough to allow theoretical understanding. In the past, for instance, some of the

*Corresponding author. Email: tkedwards@wisc.edu

achievements of the QG equations include, but are not limited to, explaining baroclinic instability (Charney 1947, 1948, Phillips 1954) and geostrophic turbulence (Rhines 1979, Salmon 1980). In particular, the QG framework allows theoretical explanations. Despite the benefits that come from QG theory, one must also keep in mind the limitations of the QG framework, since it assumes that the Froude and Rossby numbers are asymptotically small, and therefore the QG framework is an idealization of nature. With such a background, it is reasonable to hope that the behavior of water could also be amenable to some theoretical analysis, within the idealized QG framework. Here it is shown that, in a simple moist QG framework, the spectral exponent of water can take a range of values, and the spectrum can change significantly due to the influence of precipitation. Facilitating the analysis of QG water is a key observation that the water can be decomposed into contributions from two eigenmodes: the vortical mode and a moist mode.

As a quasi-geostrophic model with water, the recently derived precipitating quasi-geostrophic (PQG) equations will be used (Smith and Stechmann 2017). For comparison, there have been other variations/adaptations of the dry QG equations to include moisture and moisture effects via latent heat release, etc. (e.g., Mak 1982, Bannon 1986, Lapeyre and Held 2004, Monteiro and Sukhatme 2015); these and other models (e.g., Brennan and Lackmann 2005, Lambaerts *et al.* 2012) have provided insight into moisture dynamics and the role of latent heat release in the atmosphere. One distinguishing and advantageous property of the PQG equations is that they are asymptotic limiting equations. Specifically, the PQG equations arise in the limit of rapid rotation and strong (moist) stratification, starting from the equations for midlatitude dynamics with moisture, phase changes, and precipitation (Hernandez-Duenas *et al.* 2013).

It is worth noting some of the complicating factors that are either neglected here, or not accessible with the framework of the present paper, especially keeping in mind that the QG framework itself is asymptotic and idealized. For example, phase changes of water will be neglected, and the model here will use a crude vertical structure. While phase changes of water are undoubtedly important, it is possible to include some aspects of precipitation without including the nonlinear switch associated with phase changes; for instance, it is still possible to have coherent filamentary structures that resemble atmospheric rivers, which we analyze in a separate work (Edwards *et al.* 2019). Other studies have used more comprehensive versions of the dynamics, without neglecting some or all of the factors listed above, and are therefore able to provide a more precise connection to observational data (Spyksma and Bartello 2008, Sukhatme *et al.* 2012, Schemann *et al.* 2013, Mellado 2017). On the other hand, more comprehensive dynamics comes at the expense of complicating the possibility of a theoretical analysis like the one considered here.

The organization of the paper is as follows. In section 2, the precipitating quasigeostrophic (PQG) model is described, as well as details of the numerical method used to solve the system projected onto two vertical levels. The results from the numerical simulations of 2-level PQG are presented in section 3. section 4 provides a theoretical explanation for the exponent of the water spectra seen in the simulations. The effect of adding a meridional background gradient of water is investigated in section 5. The final section 6 contains discussion and conclusions of the main results.

2. PQG Model Description

The PQG equations can be considered as a moist version of the QG equations. The dry QG equations describe the slow evolution of synoptic-scale flows under assumptions of rapid rotation and strong stratification. Derivations for the dry QG equations can be found in Salmon (1998), Read (2007), Pedlosky (1979), Dolaptchiev and Klein (2013). Beyond the assumptions

of the dry QG framework (rapid rotation and strong dry stratification), an additional assumption in the PQG framework is a strong moist stratification of equivalent potential temperature (Smith and Stechmann 2017, Wetzel *et al.* 2017). Furthermore, in PQG, phase changes of water can be included, and the boundaries between unsaturated and saturated flow regions are represented by Heaviside nonlinear switches.

PQG is derived starting from a cloud resolving model. In principle, while any cloud microphysics scheme could be used (Smith and Stechmann 2017, Wetzel *et al.* 2019b), we focus here on warm-rain microphysics, and on a limiting case for simplicity. In brief, conversions between water vapor q_v, cloud water q_c, and rain water q_r can be modeled at macroscopic scales, and each conversion process is associated with a time scale. For evolution of mid-latitude flows on length scales of many kilometers and time scales of hours to days, the time scales for conversions of water substance are relatively short, on the order of seconds to minutes, compared to the characteristic times associated with rotation, buoyancy effects, and advection (Rogers and Yau 1989, Houze 1993, Klein and Majda 2006, Morrison and Grabowski 2008). Thus, for large-scale mid-latitude flows, the assumption of asymptotically fast cloud microphysics leads to a particularly simple model description denoted FARE, standing for the assumptions of 'fast auto-conversion and rain evaporation' (Hernandez-Duenas *et al.* 2013).

The FARE model uses the combined assumptions of both fast autoconversion and fast rain evaporation, where all microphysical processes are on the same footing as being fast relative to the dynamical time scales of interest, and it follows earlier studies that use the simplifying assumption of fast autoconversion alone (Seitter and Kuo 1983, Emanuel 1986, Bretherton 1987, Majda *et al.* 2010, Deng *et al.* 2012). When the autoconversion of small cloud droplets to rain drops is considered fast, the cloud water q_c is asymptotically small, and the state of water in the system is described by only two variables: the water vapor q_v and rain water q_r. With both fast autoconversion and fast rain evaporation, water below the saturation level exists in the vapor phase only, and water above the saturation level is instantaneously converted to rain water, which falls at constant speed V_r.

Here we focus on the structure and statistics of total water, and for simplicity consider exclusively saturated domains. One valuable aspect of a fully saturated or convecting setup is that it allows theoretical analysis that would be complicated if not impossible in the presence of phase changes or convective thresholds. Several earlier studies have also used the fully saturated or convecting setup, such as Emanuel (1986), Bretherton (1987), and Neelin and Yu (1994). An interesting case for the future is to also include the effects of phase changes as they are included in the original PQG setup (Smith and Stechmann 2017, Wetzel *et al.* 2019a), and/or to include convective effects, as done by Lapeyre and Held (2004). Here, we are presenting results without phase changes as a case that demonstrates nontrivial behavior of water in an even simpler setup. In particular, as shown below, water is influenced by two balanced eigenmodes (the vortical mode and a moist M mode), and the behavior of water is determined by the competing influences of these two eigenmodes. This competition can be seen even in a setup without phase changes; in fact, the competition is clearest to see in simulations without phase changes, since phase changes introduce additional complexity and complicate (if not prevent) theoretical analysis techniques.

In this section, we introduce the continuously stratified PQG equations in a saturated environment in section 2.1, and then the 2-level PQG equations and boundary conditions are described in detail in section 2.2. Next, we provide an overview of the numerical method and the model parameters used for our 2-level PQG simulations in section 2.3. We end the section with descriptions of the basic structures of the dry and moist variables in section 2.4.

Table 1.: Definition of variables

$\boldsymbol{x} = (x, y, z)$	Horizontal coordinates
t	Time
$\boldsymbol{u}(\boldsymbol{x}, t) = (u, v, w)$	Velocities
$\boldsymbol{u}_h = (u, v)$	Horizontal velocities
$\zeta(\boldsymbol{x}, t) = \partial_x v - \partial_y u$	Relative vorticity
$\psi(\boldsymbol{x}, t)$	Streamfunction (pressure scaled by constant density)
θ	Potential temperature
$q_v(\boldsymbol{x}, t)$	Water vapor mixing ratio
$q_r(\boldsymbol{x}, t)$	Rain water mixing ratio
$q_t(\boldsymbol{x}, t) = q_v + q_r$	Total water mixing ratio
$\theta_e(\boldsymbol{x}, t) = \theta + q_v$	Equivalent potential temperature
$PV(\boldsymbol{x}, t) = \nabla_h^2 \psi + (L/L_{ds})^2 (\partial^2 \psi / \partial z^2)$	Potential Vorticity
$M(\boldsymbol{x}, t) = q_t + G_M \theta_e$	Thermodynamic variable M

Table 2.: Dimensional parameters and typical values

L	1000km	Characteristic length scale
L_{ds}	700km	Saturated deformation
c_p	10^3 J kg^{-1} K^{-1}	Specific heat
L_v	2.5×10^6 J	Latent heat factor
$\mathrm{d}\tilde{\theta}_e/\mathrm{d}z$	1.5 K km^{-1}	Background vertical gradient of equivalent potential temperature
$\mathrm{d}\tilde{q}_t/\mathrm{d}z$	-0.6 g kg^{-1} km^{-1}	Background vertical gradient of rain water
V_T	$0.3 - 10$ m s^{-1}	Rainfall speed
U_0	10 m s^{-1}	Characteristic mid-latitude horizontal velocity
W_0	0.1 m s^{-1}	Characteristic vertical velocity
β_0	2.5×10^{-11} m^{-1} s^{-1}	Change in rate of rotation

Table 3.: Nondimensional parameters

L/L_{ds}	Nondimensional ratio of length scales
$\beta = L^2 \beta_0 / U_0$	Nondimensional change in rate of rotation
$G_M = -L_v c_p^{-1} (\mathrm{d}\tilde{q}_t/\mathrm{d}z)\ (\mathrm{d}\tilde{\theta}_e/\mathrm{d}z)^{-1}$	Ratio of the background vertical gradients of q_t and θ_e
$V_r = V_T / W_0$	Nondimensional rainfall speed

Table 4.: Notation for derivatives

$\mathrm{D}/\mathrm{D}t = \partial_t + \boldsymbol{u} \cdot \boldsymbol{\nabla}_h$	Material derivative
$\boldsymbol{\nabla}_h = \hat{\boldsymbol{x}}\, \partial_x + \hat{\boldsymbol{y}}\, \partial_y$	Horizontal laplacian
$\mathrm{D}_h/\mathrm{D}t = \partial_t + \boldsymbol{u}_h \cdot \boldsymbol{\nabla}_h$	Horizontal material derivative

2.1. *PQG equations*

Including the variation of the Coriolis parameter with latitude (the β-effect; see e.g., Read 2007), the PQG equations may be written in nondimensional form by

$$\frac{\mathrm{D}_h \zeta}{\mathrm{D}t} + \beta v = \frac{\partial w}{\partial z}\,, \tag{1a}$$

$$\frac{\mathrm{D}_h \theta_e}{\mathrm{D}t} + \frac{L_{ds}}{L} w = 0\,, \tag{1b}$$

$$\frac{\mathrm{D}_h q_t}{\mathrm{D}t} - G_M \frac{L_{ds}}{L} w = V_r \frac{\partial q_r}{\partial z}\,, \tag{1c}$$

Table 5.: Notation of variable location, where the subscript indicates which level.

$(\cdot)_1$	$(\cdot)$ at level 1
$(\cdot)_2$	$(\cdot)$ at level 2
$(\cdot)_m$	$(\cdot)$ at the mid-domain (between level 1 and level 2)

where the variables $\boldsymbol{u}(\boldsymbol{x},t), \zeta(\boldsymbol{x},t), \theta_e(\boldsymbol{x},t), q_t(\boldsymbol{x},t), q_r(\boldsymbol{x},t)$ are functions of three space dimensions $\boldsymbol{x} = (x,y,z)$ and time t; $\boldsymbol{u} = (u,v,w)$ is the fluid velocity with horizontal components $\boldsymbol{u}_h = (u,v)$; $\zeta = \partial_x v - \partial_y u$ is the vertical component of relative vorticity; θ_e is the equivalent potential temperature; q_t is the mixing ratio of total water; and q_r is the mixing ratio of rain water. With linearized thermodynamics, $\theta_e = \theta + q_v$, where $\theta(\boldsymbol{x},t)$ is the potential temperature and $q_v(\boldsymbol{x},t)$ is the mixing ratio of water vapor. The horizontal material derivative $\mathrm{D}_h/\mathrm{D}t = \partial_t + \boldsymbol{u}_h \cdot \boldsymbol{\nabla}_h$, where $\boldsymbol{\nabla}_h = \hat{\boldsymbol{x}}\,\partial_x + \hat{\boldsymbol{y}}\,\partial_y$, appears instead of the full material derivative $\mathrm{D}/\mathrm{D}t = \partial_t + \boldsymbol{u}\cdot\boldsymbol{\nabla}$, as discussed below. Summaries of the variables, parameters, and symbols are provided in Tables 1–4.

The velocity and vorticity are anomalous quantities assuming a Boussinesq background state of rest, whereas all thermodynamic quantities have been decomposed into Boussinesq background functions of altitude and anomalies; specifically, the equivalent potential temperature is $\theta_e^{tot}(\boldsymbol{x},t) = \tilde{\theta}_e(z) + \theta_e(\boldsymbol{x},t)$, the total water is $q_t^{tot}(\boldsymbol{x},t) = \tilde{q}_t(z) + q_t(\boldsymbol{x},t)$, and the rain water is $q_r^{tot}(\boldsymbol{x},t) = \tilde{q}_r(z) + q_r(\boldsymbol{x},t)$. Since the setup here is saturated, the water vapor is equal to the saturation water vapor: $q_v^{tot} = \tilde{q}_{vs}$. Conversions of water between vapor and liquid are present in the model, and, likewise, latent heating is present in the model, although these effects are implicit in (1), owing to the use of conserved variables θ_e and q_t. In this Boussinesq setting, the background gradients $\mathrm{d}\tilde{\theta}_e/\mathrm{d}z$ and $\mathrm{d}\tilde{q}_t/\mathrm{d}z$ are taken to be constants. Also, $\tilde{q}_r$ is chosen to be a constant so that $\mathrm{d}\tilde{q}_r/\mathrm{d}z = 0$ and the background states $\tilde{(\cdot)}$ are a steady state solution of (1). As a result, since $\tilde{q}_t = \tilde{q}_v + \tilde{q}_r = \tilde{q}_{vs} + \tilde{q}_r$, the gradients $\mathrm{d}\tilde{q}_t/\mathrm{d}z$ and $\mathrm{d}\tilde{q}_{vs}/\mathrm{d}z$ are equal in this setup, and the anomalous total water q_t is equal to the anomalous rain water, q_r. (See appendix A for more details.) Also, in order to maintain a saturated environment, a constant source of water is needed to balance the loss of water due to rainfall. The source of water could be taken to be a uniform constant that represents evaporation in a two-level setup, similar to the approach of Lapeyre and Held (2004), or it could be a source of rain water that enters the top of the domain, similar to the source of snow from cloud-top generating cells (Keeler *et al.* 2016a,b, 2017, Rauber *et al.* 2017) (although only warm rain is explicitly included in the present model), or an idealized source of rain water at domain top as used in other studies (e.g., Emanuel 1986, Bretherton 1987). The water source would maintain the constant background rain water $\tilde{q}_r$, and neither the water source nor the background rain water have an influence on the evolution of the anomalies in (1), so it is not needed further in what follows. In the saturated setup here, upward motion is always associated with condensation and latent heating, and downward motion is always associated with evaporation and evaporative cooling. While the environmental background state is chosen to be saturated here, it could also be chosen to be unsaturated in the more general case (Smith and Stechmann 2017).

Underlying the saturated PQG system (1) are the geostrophic and hydrostatic balances, resulting from, respectively, fast rotation and strong stable stratification:

$$\hat{\boldsymbol{z}} \times \boldsymbol{u} = -\boldsymbol{\nabla}_h \psi\,, \qquad \theta_e = \frac{L}{L_{ds}} \frac{\partial \psi}{\partial z}\,, \tag{2a,b}$$

where ψ is a streamfunction (pressure scaled by the constant density). Note that the buoyancy in (2b) depends on θ_e but does not include the dependence on water vapor and liquid water, such as water loading, that is typical of the Boussinesq and anelastic equations; this latter dependence is not included here because these effects are asymptotically small in the precipitating quasi-geostrophic limit (see Smith and Stechmann 2017, for more details). The

balances (2) may be used to rewrite the PQG equations (1) in terms of the streamfunction ψ in place of u, v, ζ, θ_e, with $\zeta = \nabla_h^2 \psi$. The geostrophic-hydrostatic balances (2) constrain the vertical velocity w to be small compared to the horizontal velocity $\boldsymbol{u}_h$, leading to dominance of horizontal advection reflected by the operator $\mathrm{D}_h/\mathrm{D}t = \partial_t + \boldsymbol{u}_h \cdot \boldsymbol{\nabla}_h$. Equations (1a,b) and (2) are mathematically equivalent to the dry quasi-geostrophic equations after replacing the saturated deformation radius L_{ds} by the dry deformation radius L_d (Salmon 1980, Read 2007, Pedlosky 1979).

In (1), there are four nondimensional parameters in the PQG equations: the length-scale ratio L_{ds}/L; change in the rotation rate with latitude, β; the rainfall speed, V_r; and the scaled ratio of the background vertical gradients of total water and equivalent potential temperature, G_M. Later on in section 5, a fifth nondimensional parameter, the meridional gradient of water, Q_y is considered. Tables 2 and 3 list the dimensional and nondimensional parameters and relationships between them.

Periodic boundary conditions are imposed in the horizontal directions, and a rigid lid boundary condition $w = 0$ is imposed at top and bottom. Applying these boundary condition to equations (1) and (2), the vertical boundary condition becomes

$$w \,=\, 0\,, \qquad \frac{\mathrm{D}_h \theta_e}{\mathrm{D}t} \,=\, 0\,, \qquad \frac{\mathrm{D}_h q_t}{\mathrm{D}t} \,=\, V_r \frac{\partial q_r}{\partial z} \tag{3a–c}$$

on both top and bottom. Further boundary conditions on q_r will also be specified such as no inflow of q_r and this is discussed further in the description of the two-level setup in section 2.2.

In what follows, we recall from the discussion between (1) and (2) that the current setup is fully saturated, so the anomaly q_r represents the same quantity as q_t:

$$q_r = q_t. \tag{4}$$

From here on, all q_r values will be replaced with q_t. Since the anomalies of rain water and total water are equivalent, we will sometimes refer simply to "the water" in what follows.

Following a similar procedure as for dry QG, the vertical velocity w may be eliminated from (1) by introducing a potential vorticity PV, which here is a moist PV based on θ_e. In addition, for PQG, one can also form a thermodynamic variable M to eliminate the vertical velocity w from (1). The PV and M variables are defined as

$$PV \,=\, \nabla_h^2 \psi + \left(\frac{L}{L_{ds}}\right)^2 \frac{\partial^2 \psi}{\partial z^2}\,, \qquad\qquad M = q_t + G_M \theta_e \tag{5a,b}$$

leading to the dynamical equations

$$\frac{\mathrm{D}_h PV}{\mathrm{D}t} + \beta v \,=\, 0\,, \qquad\qquad \frac{\mathrm{D}_h M}{\mathrm{D}t} \,=\, V_r \frac{\partial q_t}{\partial z}\,. \tag{6a,b}$$

For the PQG system, there are coupled equations (6) for PV and M, the latter which is simply the combination of (1b,c) that eliminates w within this framework.

The form of PQG in (6) highlights the two eigenmodes of the system: a vortical mode characterized by PV and a moist eigenmode characterized by M. The water can be decomposed into its contributions from these two eigenmodes as

$$q_t \,=\, M - G_M \theta_e \tag{7}$$

which follows from (5b), and where $\theta_e = (L/L_{ds})\partial\psi/\partial z$ is the contribution from the vortical mode. From this decomposition, one can see that the behavior of water is complicated by the competing contributions from these two eigenmodes. At the same time, this eigenmode decomposition will be useful below for sorting out the behavior of water.

2.2. *Two-level PQG*

There are several derivations of the dry two level QG equations, such as in Phillips (1954), Salmon (1998). Here we include a detailed derivation of PQG to make clear how the discretized equation for M is obtained, and how we implement boundary conditions for q_t and M.

According to the two-level set-up shown in figure 1, we use the notation $\mathrm{D}_1(\cdot)/\mathrm{D}t = \partial_t(\cdot) + u_1\partial_x(\cdot) + v_1\partial_y(\cdot)$, and similarly for $\mathrm{D}_2(\cdot)/\mathrm{D}t$ and $\mathrm{D}_m(\cdot)/\mathrm{D}t$. Using a finite difference approximation in z of (6) and specific initial/boundary conditions described below, we arrive at the two level PQG equations given by

$$\frac{\mathrm{D}_1 PV_1}{\mathrm{D}t} + \beta v_1 \,=\, 0\,, \qquad\qquad \frac{\mathrm{D}_2 PV_2}{\mathrm{D}t} + \beta v_2 \,=\, 0\,, \tag{8a,b}$$

$$\frac{\mathrm{D}_m M_m}{\mathrm{D}t} \,=\, -\frac{V_r}{\Delta z} q_{t,m} \,=\, -\frac{V_r}{\Delta z}(M_m - G_M\theta_{e,m})\,, \tag{8c}$$

with

$$PV_1 \,=\, \nabla_h^2\psi_1 + \left(\frac{1}{\Delta z}\frac{L}{L_{ds}}\right)^2(\psi_2 - \psi_1)\,, \tag{9a}$$

$$PV_2 \,=\, \nabla_h^2\psi_2 + \left(\frac{1}{\Delta z}\frac{L}{L_{ds}}\right)^2(\psi_1 - \psi_2)\,, \tag{9b}$$

$$\theta_{e,m} \,=\, \frac{L}{L_{ds}}\frac{\psi_2 - \psi_1}{\Delta z}\,, \tag{9c}$$

$$u_i \,=\, -\frac{\partial\psi_i}{\partial y}\,, \qquad\qquad v_i \,=\, \frac{\partial\psi_i}{\partial x} \qquad \text{for } i = 1, 2\,, \tag{9d,e}$$

$$u_m \,=\, \tfrac{1}{2}(u_1 + u_2)\,, \qquad\qquad v_m \,=\, \tfrac{1}{2}(v_1 + v_2)\,. \tag{9f,g}$$

In quasigeostrophic literature, the velocities u_m, v_m are also known as the barotropic (depth-averaged) velocities. Expressions (9a-c) are obtained by a centered difference in z of (6a) with

$$\frac{\partial^2\psi}{\partial z^2} \,\approx\, \frac{1}{\Delta z}\left(\left.\frac{\partial\psi}{\partial z}\right|_{z=z_m} - \left.\frac{\partial\psi}{\partial z}\right|_{z_B}\right) \qquad \text{for level 1} \tag{10a}$$

$$\frac{\partial^2\psi}{\partial z^2} \,\approx\, \frac{1}{\Delta z}\left(\left.\frac{\partial\psi}{\partial z}\right|_{z_T} - \left.\frac{\partial\psi}{\partial z}\right|_{z=z_m}\right) \qquad \text{for level 2} \tag{10b}$$

and where z_B, z_m, z_T denote z at the bottom, middle and top, respectively. For an initial condition of $\theta_e = 0$ at top and bottom, equation (3b) ensures that the value will remain zero for all time, and hence that $\partial\psi/\partial z|_{z_T} = \partial\psi/\partial z|_{z_B} = 0$ for all time by (2b). For the more general vertical boundary condition $\mathrm{D}_h\theta_e/\mathrm{D}t = 0$, it was shown that the interior two-level dry QG equations are unchanged (Phillips 1954, Salmon 1998). The same result also holds for the 2-level PQG equations within a single phase, either unsaturated or saturated, but not in an environment with phase changes. For simplicity, and since we consider a domain that is completely saturated for all time, we use the vertical boundary condition $\theta_e = 0$ as done similarly in the dry QG case (e.g. in Held and O'Brien (1992)).

To obtain (8c), an upwind difference was taken to approximate (6b). For example at z_m, $\partial/\partial z\,(M - G_M\theta_e)\,|_{z=z_m} \approx V_r/\Delta z\,(q_t|_{z=z_T} - q_t|_{z=z_m})$. Imposing the initial condition that $q_t(t=0) = 0$ for $z \geq z_T$, the upwind approximation of equation (3c) gives $q_t(z = z_T) = 0$ for all time. From this latter condition,

$$\frac{\partial}{\partial z}\,(M - G_M\theta_e)\,|_{z=z_m} \approx \frac{V_r}{\Delta z}\,(0 - (M_m - G_M\theta_{e,m}))\,. \tag{11}$$

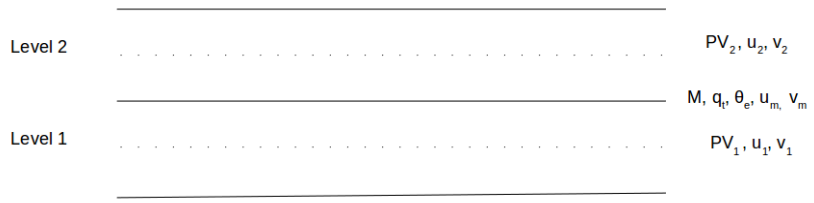

Figure 1.: Diagram of the two-level set-up. The variables q_t, M, θ_e are in fact $q_{t,m}, M_m, \theta_{e,m}$, the indices were dropped here so as to match the variables in the later sections.

Since the main interest is on the dynamics of the moist variables in the interior (M_m and $q_{t,m}$), and because the moist variables at the lower boundary do not affect the values of the moist variables in the interior, the M-equation at the lower boundary is omitted. To simplify notation, the subscript m will be dropped from θ_e, M from here on.

To summarize, the two-level PQG system, under saturated conditions without phase changes, takes the form shown in (8)–(9), which is the standard Phillips model plus a tracer (M), where the tracer M is advected by the barotropic velocity and adjusts with the relaxation rate $V_r/\Delta z$ to the baroclinic (equivalent potential) temperature (weighted with factor G_M). The tracer M is passive in this setup of saturated conditions without phase changes, in the sense that the evolution of the upper- and lower-level PVs can be found without knowledge of the evolution of M. Two things which are different with respect to canonical studies of passive tracers in QG turbulence are that the tracer is not advected by velocities in the layers, but by the vertically averaged (barotropic) velocity, and the tracer is relaxing to the baroclinic (equivalent potential) temperature (weighted with factor G_M).

2.3. *Discretized model for numerical computations*

Our main goal is to investigate the structure and statistics of water in a statistically quasi-steady state of saturated PQG, evolving from baroclinically unstable initial conditions. To this end, we numerically computed the solution to (8) with additional dissipation terms given by 4th-order hyperviscosity and lower-level friction:

$$\frac{\mathrm{D}_1 PV_1}{\mathrm{D}t} - U\partial_x PV_1 + v_1 \partial_y PV_{1,bg} + \beta v_1 \;=\; -\,\kappa_M \Delta\psi_1 - \nu\Delta^4 PV_1\,, \tag{12a}$$

$$\frac{\mathrm{D}_2 PV_2}{\mathrm{D}t} + U\partial_x PV_2 + v_2 \partial_y PV_{2,bg} + \beta v_2 \;=\; -\,\nu\Delta^4 PV_2\,, \tag{12b}$$

$$\frac{\mathrm{D}_m M}{\mathrm{D}t} + v_m \partial_y M_{bg} \;=\; -\,\frac{V_r}{\Delta z}\left(M - G_M\theta_e\right) - \nu\Delta^4 M\,. \tag{12c}$$

The parameter values $U = 0.2$, $\beta = 2.5$, $\kappa_M = 0.05$, $\nu = 5\times10^{-15}$ and $k_{ds} = 4$ were chosen to match the (dry) mid-latitude atmosphere case studied in Qi and Majda (2016). The expressions for the background values of θ_e and PV are, respectively, $\theta_{e,bg} = \Theta y = -\left(1/\Delta z\right)\left(L/L_{ds}\right)\left(2Uy\right)$ and $PV_{j,bg} = (-1)^j\left(1\Delta z\right)^2\left(L/L_{ds}\right)^2\left(2Uy\right)$. The parameters reflecting the presence of water in our 2-level PQG equations are G_M and V_r: G_M depends on the background water profile and V_r is the rainfall speed. In the present study, we fix the value $G_M = 1$ and vary V_r. The baseline case considered in sections 3 and 4 has background meridional gradient $Q_y = 0$ such that $M_{bg} = (Q_y + G_M\Theta)y = G_M\Theta y$; $Q_y \neq 0$, $G_M \neq 1$ is considered in section 5.

A pseudospectral solver was used to solve (12) on a doubly periodic, horizontal domain. The time-stepping was done according to a 3rd-order Runge-Kutta scheme with an adaptive Δt chosen to satisfy the CFL condition. Three-halfs padding was used for de-aliasing. Most

of the simulations used resolution $N^2 = 512^2$ Fourier modes, with a few higher-resolution simulations as described below. The initial condition was a band of eigenmodes centered around the unstable wave-vector $(k, l) = (3, 1)$, and the simulations were run long enough to obtain statistical steady states. These eigenmodes can be obtained by solving the linearized equation (see appendix C for more details on the linearized equations and initial condition setup). In addition to the two modes obtained from the PV equations, as done in dry QG, there is another eigenmode from the M equation that is not present in dry QG.

2.4. *Basic structure of the statistical steady state (baseline case)*

We end this section with figure 2 of zonally averaged variables in a time interval $t \in [60, 100]$, in part to demonstrate that the chosen parameter values for β, deformation radius k_{ds}^{-1}, and background vertical shear U are consistent with mid-latitude dynamics. Zonal averages are denoted by an overbar, e.g., the zonally averaged zonal velocity at mid-height is denoted $\bar{u}_m(t, y)$. Figure 2 will also help with interpretation of later single-time plots visualizing the water variables q_t and M in the (x, y)-plane.

Figure 2a shows a single, persistent, eastward jet with minimal meandering in this relatively short time window; some meandering is observed for longer time windows as for the mid-latitude case of Qi and Majda (2016). The asymmetry in the jet, with the westward jet being broader and the eastward jet being narrower, is related to the β effect (e.g., Kuo 1949, Armi 1989). The potential temperature shown in figure 2b is approximately constant below and above the jet, which separates warm air to the south from colder air to the north. There is a gradient of decreasing temperature across the jet region. Within the saturated one-phase PQG approximation, the dynamics of ψ, and hence the dynamics of velocity $\boldsymbol{u}$ and temperature θ_e, are not changed by the presence of water. Thus figures 2a and 2b are the same for all values of rainfall speed V_r. However, the dynamics of the water variables q_t and M depend crucially on V_r as will be demonstrated in the following sections. For $V_r = 0.1$, the large-scale features of $\bar{M}(t, y)$ roughly mirror the features of $\bar{\theta}_e(t, y)$, but with more fine-scale structure (figure 2c). The zonally averaged anomalous water q_t is concentrated at the boundaries of the jet, with less water on the southern warm side and more water on the northern cold side (figure 2d). A more detailed analysis of zonally averaged water and meridional water fluxes is planned for a forthcoming manuscript.

To view the simulations from a PV perspective, the power spectra for PV_1, PV_2 and kinetic energy at level 1,2 as well as the potential energy are presented in figure 3b. The simulations for this paper are in the forward enstrophy cascade regime, with the KE spectra matching those found in Qi and Majda (2016), also in the forward cascade regime. If simulations were run in a different regime, a regime with the inverse cascade, one would expect a different shape, notably a flatter KE spectra with a -5/3 slope, such as those found in (Larichev and Held 1995, Smith and Vallis 2001).

3. Simulation results for water variables

In this section, the variability of water is investigated, and it is illustrated in terms of both its physical-space structure (section 3.1) and its power spectral density (section 3.2). A main goal is to explore how the water variability changes (if at all) as the influence of precipitation changes, as controlled in the model here by the parameter V_r.

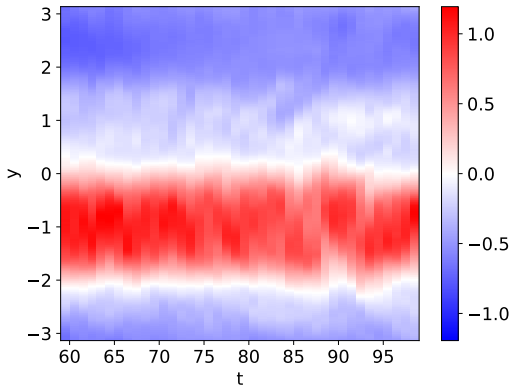

(a) $\bar{u}_m(t, y)$

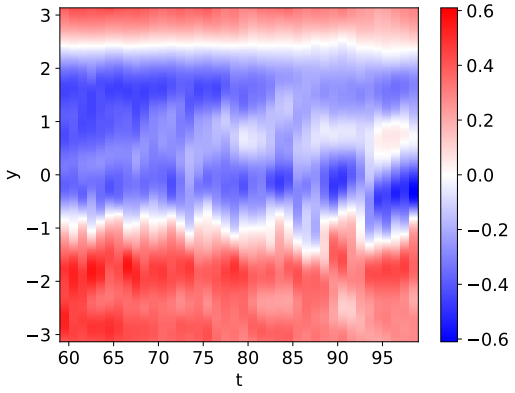

(b) $\bar{\theta}_e(t, y)$

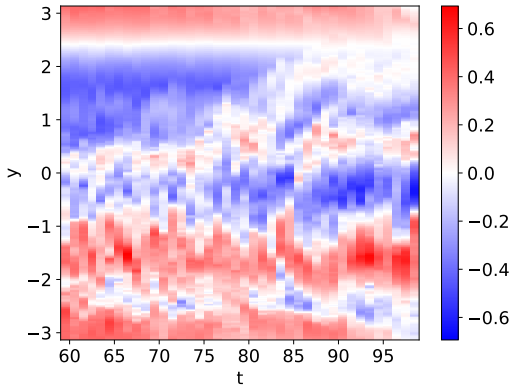

(c) $\bar{M}(t, y)$ for $V_r = 0.1$

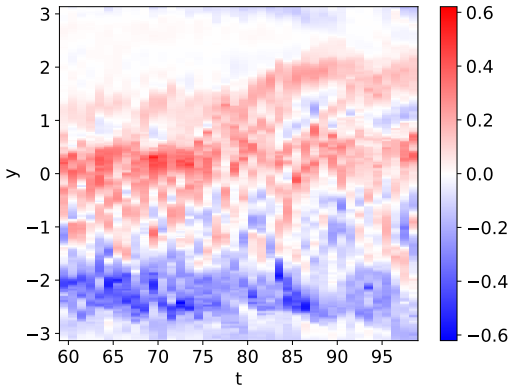

(d) $\bar{q}_t(t, y)$ for $V_r = 0.1$

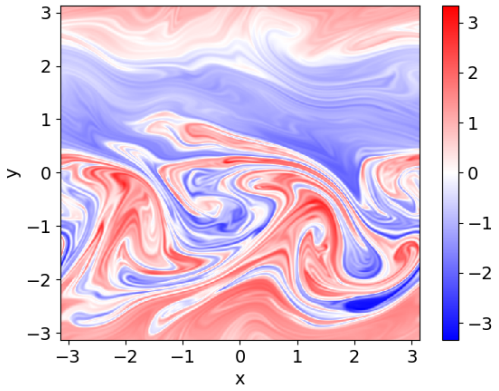

(e) Snapshot of PV_1

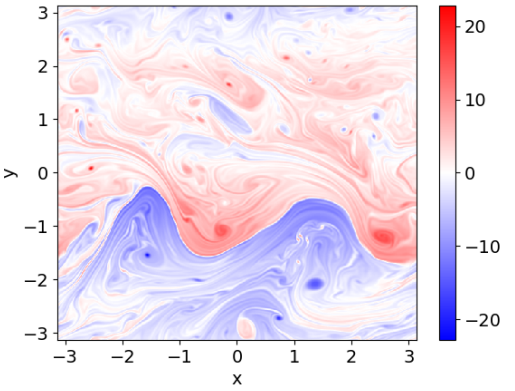

(f) Snapshot of PV_2

Figure 2.: Panels (a)-(d) show zonally averaged quantities as a function of time t and meridional direction y: (a) zonal velocity $\bar{u}_m$, (b) equivalent potential temperature $\bar{\theta}_e$, (c) $\bar{M}(t, y)$ for $V_r = 0.1$, (d) total water $\bar{q}_t$ for $V_r = 0.1$, and (e) snapshot of PV_1 at $t = 60$ (f) snapshot of PV_2 at $t = 60$. One time unit corresponds to about one day. (Color online)

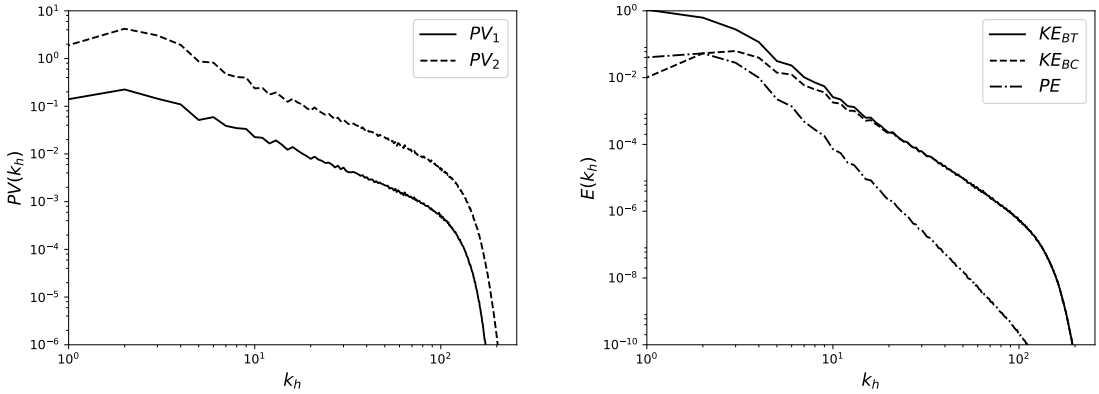

(a) Spectra of PV_1, PV_2 (b) Spectra of KE_1, KE_2, PE

Figure 3.: Panels (a), (b) show the spectra of (a) PV_1, PV_2 and (b) Kinetic Energy at level 1, KE_1 and level 2, KE_2 and Potential Energy, PE.

3.1. *Physical-space structure*

Single-time snapshots of anomalous water q_t are shown in figure 4, where the different rows correspond to different values of rainfall speed $V_r = 0, 0.1, 1.0$. The time is $t = 60$, after the simulation has reached a statistically steady state, and the height is mid-level between levels 1 and 2 (see figures 1 and 2). One can see that both the amplitude and variability of water depend strongly on V_r, with both amplitude and fine-scale structure decreasing as V_r increases.

From the q_t plots in figure 4, one anticipates that variance spectra for water q_t will steepen as rainfall speed V_r increases and fine-scale structure decreases. In the next section 3.2, we quantify the range of spectral scalings and the limiting spectral exponents for $V_r \to 0$ and $V_r \to \infty$. Later in section 4, we provide a rational basis for understanding the structural transition from $q_t \sim M$ for $V_r \to 0$, to $q_t \sim w$ for $V_r \to \infty$.

3.2. *Spectra of total water*

Figure 5 shows that the spectra of total water variance steepen and decrease in magnitude as rainfall speed V_r increases, reflecting the loss of fine-scale structure in q_t as well as the amplitude reduction seen in figure 4. To quantify the changes in the spectra, figure 6 shows the spectral exponents as a function of V_r. (The spectral exponents were computed by a linear fit from $k_h = 30 \pm 5$ to $k_h = 70 \pm 5$, shown as vertical lines to indicate uncertainty in the figure; the horizontal lines are the spectral exponents computed from $k_h = 30$ to 70.) Broadly speaking, there seem to be three distinct regimes: the spectral exponent approaches the value ≈ -1.4 as $V_r \to 0$; there is a transition region for $10^{-2} < V_r < 1$; the exponent approaches the bottom dashed blue line as $V_r \to \infty$, with value close to -4.

A detail that arises in figure 6 is the non-monotonic change in the spectral exponent as a function of V_r. For V_r values between roughly 10^0 to 10^1, the spectral exponent value falls below the large-V_r limiting value (about -4). To investigate whether the non-monotonicity is a numerical artifact, higher-resolution simulations were carried out with resolution of 1024^2 Fourier modes (as opposed to the standard cases with 512^2 Fourier modes), and the results are shown in figure 6 by the green marks. The higher-resolution results appear to be only slightly more monotonic, which suggests the non-monotonicity may be a natural property of the system.

Observational studies, for comparison, have reported spectral exponents that range as widely

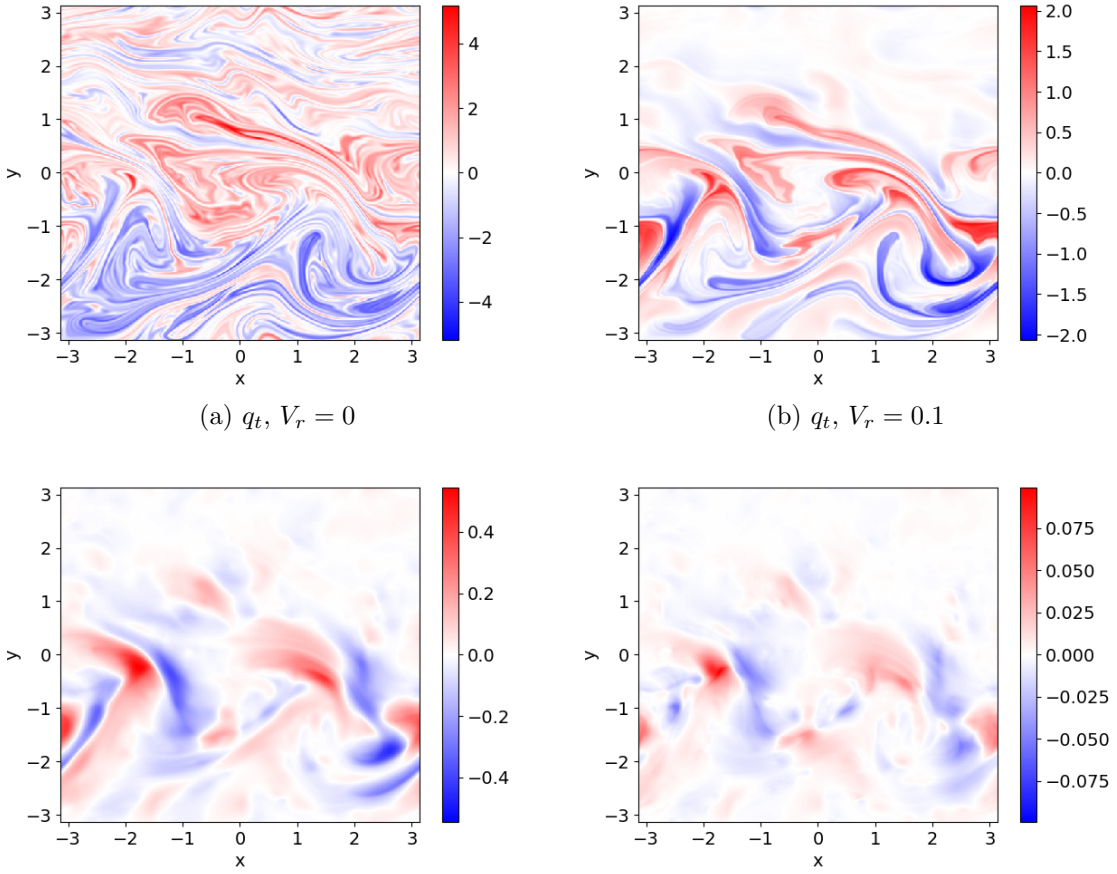

(a) q_t, $V_r = 0$ (b) q_t, $V_r = 0.1$

(c) q_t, $V_r = 1$ (d) q_t, $V_r = 10$

Figure 4.: Contours of total water q_t for increasing V_r at time $t = 60$, after quasi-steady state has been established. (Color online)

as -1.3 to -2.7 (Fischer *et al.* 2012) or -1.4 to -2.2 (Kahn and Teixeira 2009), although the more convenient numbers of $-5/3$ and -2 are more commonly reported. Such observational ranges are more narrow than the wide range of roughly -1.4 to -4 shown in figure 6 for the model. Nevertheless, it is interesting that the model's bound of -1.4 is roughly in line with the bound that is seen in observations. Moreover, in the model a steeper spectrum can also be seen, and it is due to the influence of precipitation.

The observational spectra are influenced by numerous factors, and not all factors are included in the present idealized setup. In the present setup, it is mainly three parameters that could potentially influence the water spectrum: rainfall (V_r), vertical moisture gradient, and meridional moisture gradient. The latter two (the moisture gradients) will be shown in section 5 to have limited influence on the water spectrum. Rainfall, on the other hand, is seen to have a significant influence on the water spectrum.

To aid the comparison between observations and the present idealized model, the parameter V_r here can be viewed as an indicator of the influence of precipitation on the variability of water, in the following way. While the origin of the parameter V_r is as a representation of terminal velocity of rain, the case of $V_r = 0$ here is equivalent to the dynamics of a moist atmosphere that is always unsaturated and cloud-free. As a result, small V_r values correspond to dynamics with little or no influence of precipitation, moderate V_r values correspond with appreciable influence of precipitation, and large V_r values correspond with a dominating in-

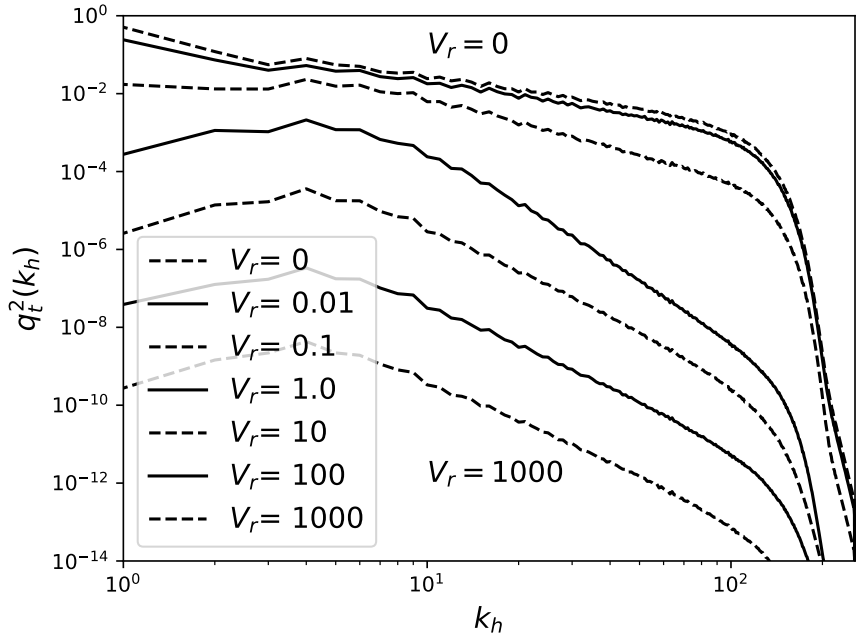

Figure 5.: Spectra of total water q_t for different values of rainfall speed V_r.

fluence of precipitation. The correspondence between V_r in this saturated model and V_r in nature is not a perfect match, since the model here is saturated whereas nature has phase changes of water. Nevertheless, the trends in the influence of V_r on water spectra can offer an idealized indication of trends in the influence of precipitation on water spectra.

Given this viewpoint of V_r, and given all of the factors that complicate a perfect comparison between observations and the present idealized model, it is interesting that roughly -1.4 is seen as the bound on the spectral exponent in both observations and the model, and it is seen in the model for the case of small V_r, indicating little or no influence of precipitation. Beyond this bound, steeper spectra are also seen in both observations and the present idealized model. While the steeper spectra in the model are mainly due to a larger influence of precipitation (as indicated by larger V_r values), one can expect that the steeper spectra in observations are likely influenced by precipitation as well as numerous other factors. Also, while a large range of V_r values was used here in order to explore the limiting cases, it is a smaller range of V_r values (roughly a factor of 10) that causes the large changes in the spectral exponent, ranging from -1.4 to -4 or even steeper.

From a broad point of view, the results here suggest that, even with a minimal model such as PQG, it is possible to see a wide range of exponents, broadly similar to the existence of ranges of exponents in observational data, rather than a unique, universal exponent.

4. Limiting values for water spectral exponents

In section 3, it was seen in figure 6 that the behavior of water changes significantly as the influence of precipitation changes, as measured by changes in V_r. In particular, the spectral exponent of q_t^2 approaches different limiting values as $V_r \to 0$ and $V_r \to \infty$. In this section, we present some theoretical explanations to better understand this behavior.

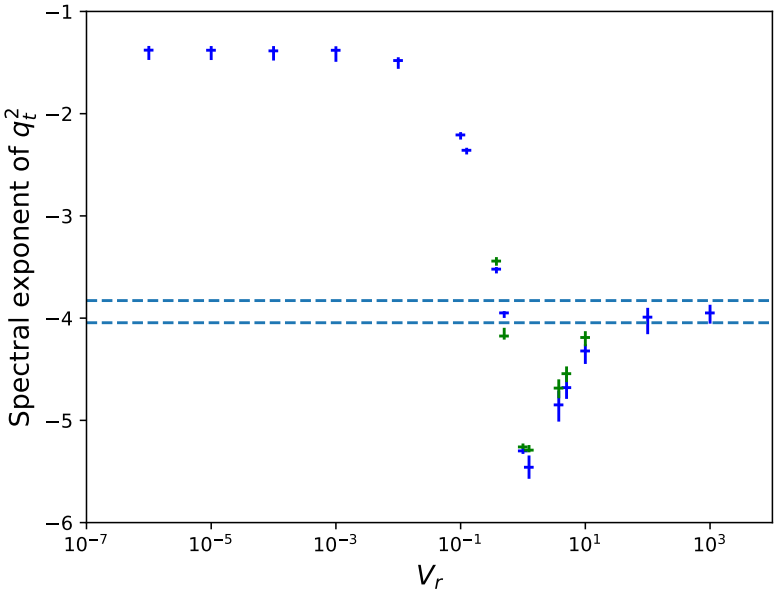

Figure 6.: Spectral exponents of q_t^2 for increasing V_r. Runs with a resolution of 512^2 Fourier modes are in blue and those of 1024^2 are in green. Error bars are indicated by the vertical line segments. The dashed horizontal lines are explained in section 4.2. (Color online)

4.1. *Small rainfall speed*

A rudimentary understanding of the limit $V_r \to 0$ can be found from setting $V_r = 0$ in the continuously stratified PV-M equations (6) with $\beta = 0$. There is a well-known analogy between the PV-equation (6a) and the vorticity equation for 2D turbulence (Charney 1971). By the analogy, one may predict the scalings for the kinetic energy $KE(k_h)$ (associated with velocity) and potential energy $PE(k_h)$ (associated with θ_e) resulting from the forced-dissipative version of (6). The theory relies on isotropy and the existence of inertial ranges in a statistically steady state (Kraichnan 1967). In the inertial range of scales smaller than the forcing scales and larger than the dissipation scale, these predictions are $KE(k_h) \propto k_h^{-3}$ and $PE(k_h) \propto k_h^{-5}$, where the latter uses the relations between $\boldsymbol{u}, \psi, PV$ and θ_e given by (2) and (5a).

The M-equation (6b) with $V_r = 0$ describes the evolution of a passive scalar M advected by the horizontal winds, with expected shallow spectrum $M^2(k_h) \propto k_h^{-1}$ (e.g., Babiano *et al.* 1987). Figure 7(a) and figure 8 reflect this fact as well. The latter figure is made in the same way as that described in subsection 3.2 for figure 6. (The notation of $M^2(k_h), q_t^2(k_h)$ will be used to describe the power spectra of M, q_t in terms of the horizontal wavenumber.)

In the discretized 2-level equations with hyperviscosity (12a,b), the Phillips background acts as a large-scale forcing, albeit anisotropic, leading to baroclinic instability and eventually to a statistically steady state. In previous studies of both forced-dissipative 2D turbulence with $\beta \neq 0$ (e.g., Maltrud and Vallis 1991) and 2-level QG-equations with $\beta \neq 0$ (e.g., Qi and Majda 2016), the spectrum has been observed to be $KE \propto k_h^q$ with $-4 < q < -3$. As discussed in the latter references and many others, the anisotropy introduced by nonzero β leads to a change in flow structure from vortices to anisotropic jets, and as reproduced here in figure 2. Hence, the arguments surrounding the scalings $KE \propto k_h^{-3}$, $PE \propto k_h^{-5}$ and $M^2 \propto k_h^{-1}$ are no longer strictly valid, but the observed spectra are nevertheless not far from the predictions associated with isotropic conditions. Our simulations of (12) show, approximately, $KE \propto k_h^{-3.8}$, $PE \propto k_h^{-5.8}$ and $M^2 \propto k_h^{-1.4}$. Factors contributing to steeper-

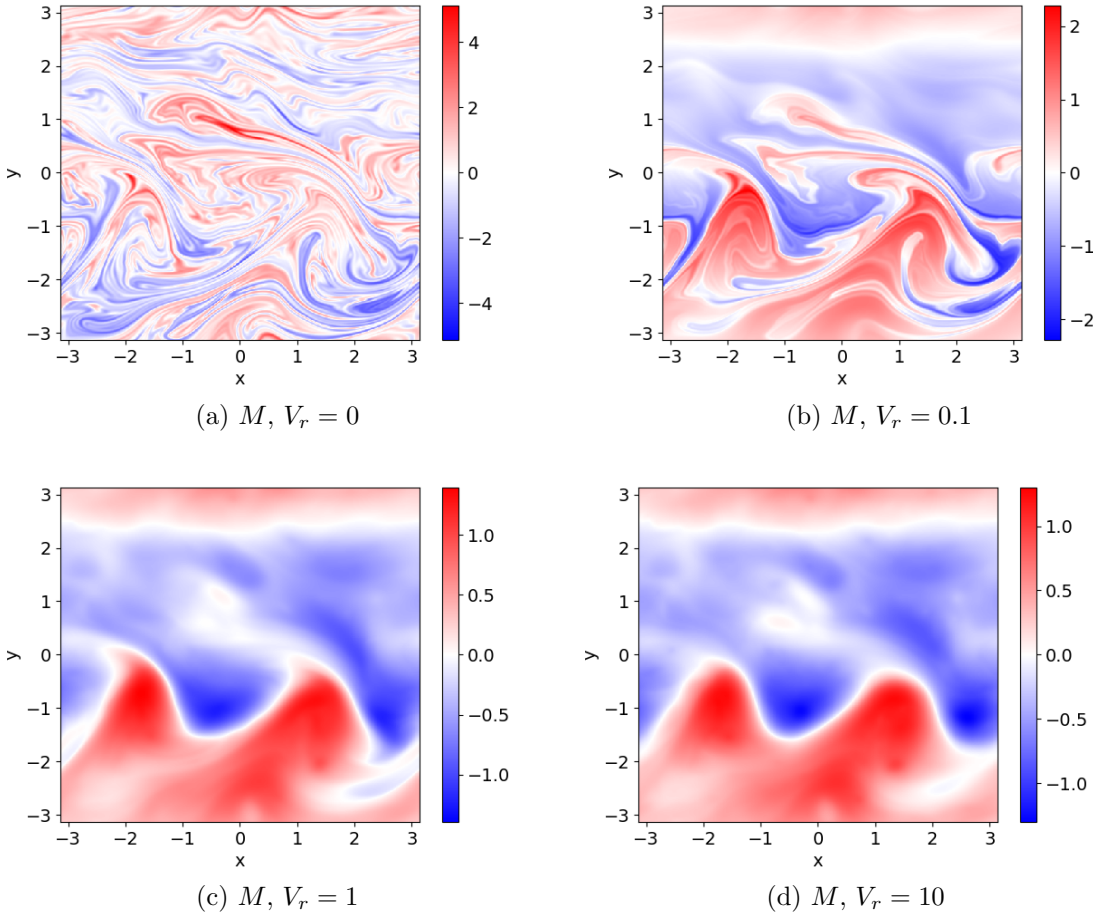

(a) M, $V_r = 0$ (b) M, $V_r = 0.1$

(c) M, $V_r = 1$ (d) M, $V_r = 10$

Figure 7.: Contours of M for increasing V_r at time $t = 60$, after quasi-steady state has been established. (Color online)

than-isotropic spectra are anisotropy, structure formation and truncated vertical structure.

Finally, we can use the information about the spectral scalings for $PE(k_h)$ and $M^2(k_h)$ together with relation $q_t = M - G_M\theta_e$ to understand the spectral scaling of q_t observed in figure 6 for $V_r \to 0$. Since the potential energy spectrum $PE(k_h)$ falls off much more rapidly than the M-spectrum $M^2(k_h)$, it is clear that significantly more 'energy' is associated with M than with θ_e as soon as wavenumbers k_h are larger than the forcing scales k_f, which are the largest scales in our simulation domain. Hence, q_t inherits the fine-scale structure of M as $V_r \to 0$, and the spectrum of q_t scales as $q_t^2 \propto k_h^{-1.4}, k_h > k_f$.

4.2. *Large rainfall speed*

Consider the discretized version of equation (1c) for q_t at mid-height in the 2-level set-up:

$$\frac{\mathrm{D}_m q_t}{\mathrm{D}t} - G_M \frac{L_{ds}}{L} w + v Q_y \;=\; -\frac{V_r}{\Delta z} q_t \,. \tag{13}$$

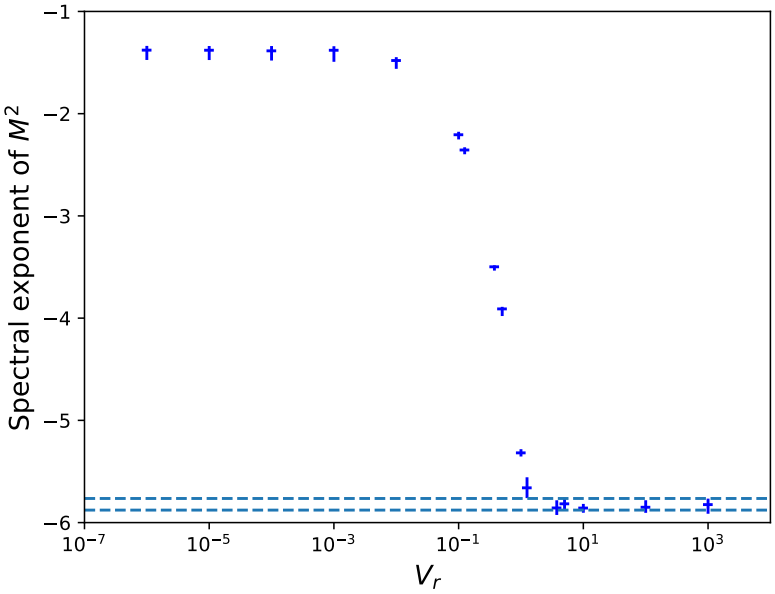

Figure 8.: Spectral exponents of M_t^2 for increasing V_r. Runs with a resolution of 512^2 Fourier modes are in blue. Error bars are indicated by the vertical line segments. The dashed horizontal lines indicate the computed spectral exponent for θ_e^2 (there are two lines to indicate uncertainty). (Color online)

We set $Q_y = 0$ for the baseline case considered above in figures 2-6. Defining $\epsilon = 1/V_r$, the variables in (13) can be expanded in powers of ϵ, for example,

$$q_t = q_t^{(0)} + \epsilon q_t^{(1)} + \cdots , \tag{14a}$$

$$\psi = \psi^{(0)} + \epsilon \psi^{(1)} + \cdots , \tag{14b}$$

$$w = w^{(0)} + \epsilon w^{(1)} + \cdots , \tag{14c}$$

and so on. The order $\mathrm{O}(\epsilon^{-1})$ balance gives

$$0 = -\frac{V_r}{\Delta z} q_t^{(0)} . \tag{15}$$

To leading order, then, the total water q_t is small, and its contribution at next order, $q_t^{(1)}$, satisfies the balance

$$-G_M \frac{L_{ds}}{L} w^{(0)} = -\frac{V_r}{\Delta z} q_t^{(1)} . \tag{16}$$

(For a more formal derivation where this limit is included as part of the distinguished limit for PQG, see Smith and Stechmann 2017).

Accordingly, in our simulations with large V_r, we observe that the magnitude of q_t becomes small, and $q_t \sim w$, as in the time snapshot figure 9 with $V_r = 10$. Similarly, the spectral scaling exponent for the spectrum of q_t^2 approaches the exponent characterizing the spectrum w^2 as seen in figure 6.

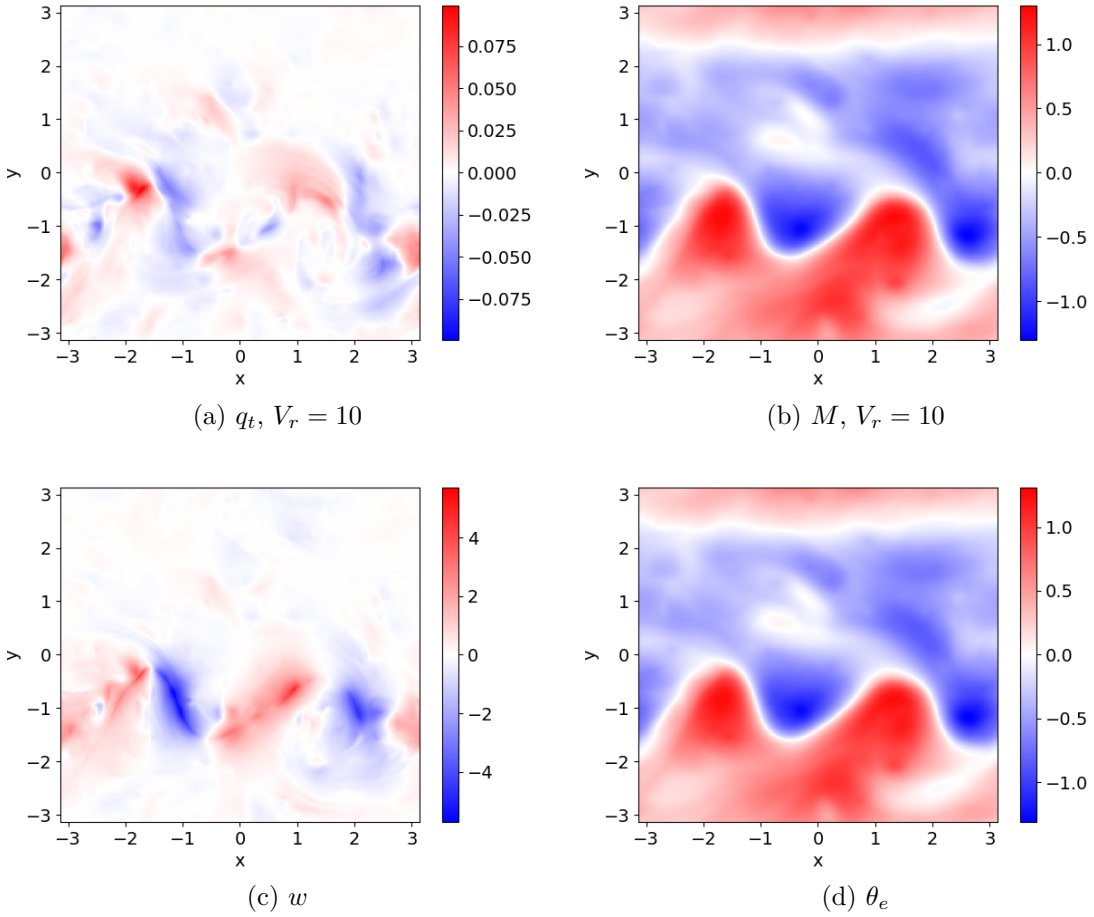

(a) q_t, $V_r = 10$ (b) M, $V_r = 10$

(c) w (d) θ_e

Figure 9.: Contours of (a) total water q_t, (b) M, (c) vertical velocity w, and (d) equivalent potential temperature θ_e; the rainfall speed is fixed at $V_r = 10$. For this large V_r, the structure of q_t is similar to the structure of w; M approaches θ_e. (Color online)

4.3. *Intermediate V_r values*

Between the small V_r and large V_r values, the spectral exponent of q_t exhibits a wide range of values as seen in (6). As pointed out in section 3.2, the non-monotonocity due to the dip is perhaps an unexpected result; is this dip a numerical artifact or is it not and if so, why does this dip occur?

As mentioned above, the dip is believed to be a natural property of the system from results from other higher resolution simulations. Further evidence is provided by comparison with the spectral exponent of θ_e and M, as shown in figure 8. Since $q_t = M - G_M\theta_e$, the spectral slope of q_t will match the shallower slope of M, which persists until around $V_r = 1$. When V_r is approximately 1, the exponent of M is approaching -5.5 or -6, which explains why the spectral exponent of q_t is able to also reach approximately -5.5.

5. Effects of a meridional and vertical moisture gradients

In addition to precipitation, other factors can also influence the water variance spectrum. Two such factors are the meridional moisture gradient, associated with parameter Q_y, and the vertical moisture gradient, associated with parameter G_M.

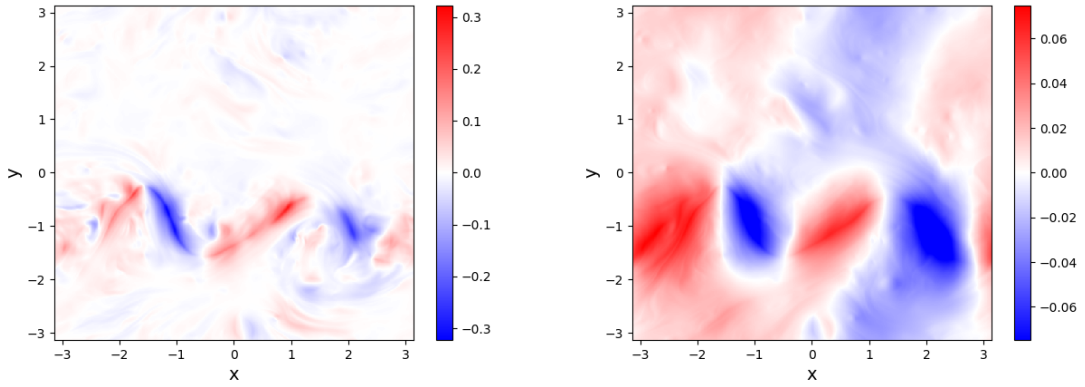

(a) $G_M(L_{ds}/L)w$ (b) $-Q_y v_m$

Figure 10.: Winds at mid-height: (a) w and (b) v_m. (Color online)

The effect of meridional moisture gradient can be studied by taking $Q_y \neq 0$ in (13). We explored several values of Q_y corresponding to $|Q_y| << G_M L_{ds}/L$, $|Q_y| \approx G_M L_{ds}/L$, and $|Q_y| >> G_M L_{ds}/L$.

We observed that the effects of Q_y are the most apparent for large V_r, and thus we present only this case. Returning to (13), the scaling $V_r = \mathrm{O}(\epsilon^{-1})$ with $\epsilon \to 0$ gives $q_t^{(0)} = 0$ and the O(1) balance

$$v^{(0)} Q_y - G_M \frac{L_{ds}}{L} w^{(0)} = -\frac{V_r}{\Delta z} q_t^{(1)} . \tag{17}$$

Now $q_t^{(1)}$ is a combination of $v^{(0)}$ and $w^{(0)}$. By changing the coefficients Q_y and $G_M L_{ds}/L$, the structure of q_t may inherit the structure of w, or the structure of v, or some combination of the two.

Single-time snapshots of w and v_m at mid-height are plotted in figure 10, so that their structure can be compared to q_t. Note that the structure of the winds does not depend on the value of V_r because of the one-way coupling. For fixed, large $V_r = 10$, figure 11 illustrates the competition between w and v for determining the structure of q_t, depending on the value of background meridional water gradient Q_y compared to $G_M L_{ds}/L$. Figure 11a is the baseline case with $Q_y = 0$, showing that q_t inherits the structure of w seen in figure 10a. However, figure 11b for $|Q_y| \approx G_M L_{ds}/L$, shows that q_t inherits the structures of both v and w. While not as easy to see, the effects of w can be observed in figure 11b, for example in the lower right corner near $x = 1, y = -3$, there is a streak through the negative anomaly in q_t corresponding to the weak positive anomalies in w. The dual dependence of q_t on w and v can also be observed in spectra as shown in figure 12. For comparison to q_t^2, the spectra for w^2 and v^2 have been normalized by the appropriate coefficients from (17). For $1 \leq k_h \leq 5$, Q_y causes the q_t^2 spectra to have a similar shape to that of the v^2 spectra. However, for large k_h, the shape of the q_t^2 spectra seems to independent of Q_y. In this case of $V_r = 10$, where the rainfall speed is large, yet not so large to be near the asymptotic regime, both the q_t^2 spectra are between the normalized v^2 and w^2 spectra. If a larger value of V_r is taken, both of the q_t^2 spectra approach that of the w^2 spectra, for large k_h. One sees that the background meridional water gradient Q_y is another parameter, in addition to the parameters of the dry system and rainfall speed, V_r, which can change the characteristics of the spectral scaling for total water q_t.

Another water parameter, G_M can also effect the spectral scaling of total water. From (13), it can be seen that G_M does not have as strong an effect on the shape of the spectral curves for q_t.

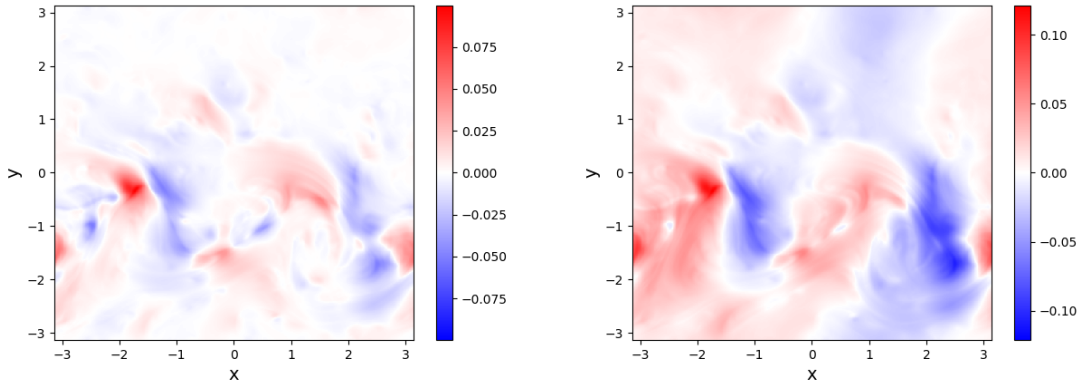

(a) q_t with $Q_y = 0$ (b) q_t with $Q_y = -1$

Figure 11.: Contours of total water q_t for large $V_r = 10$: (a) $Q_y = 0$ corresponding to Phillips background with zero background meridional water gradient; (b) $|Q_y| = 1$ corresponding to Phillips background with large gradient of water in the meridional direction. (Color online)

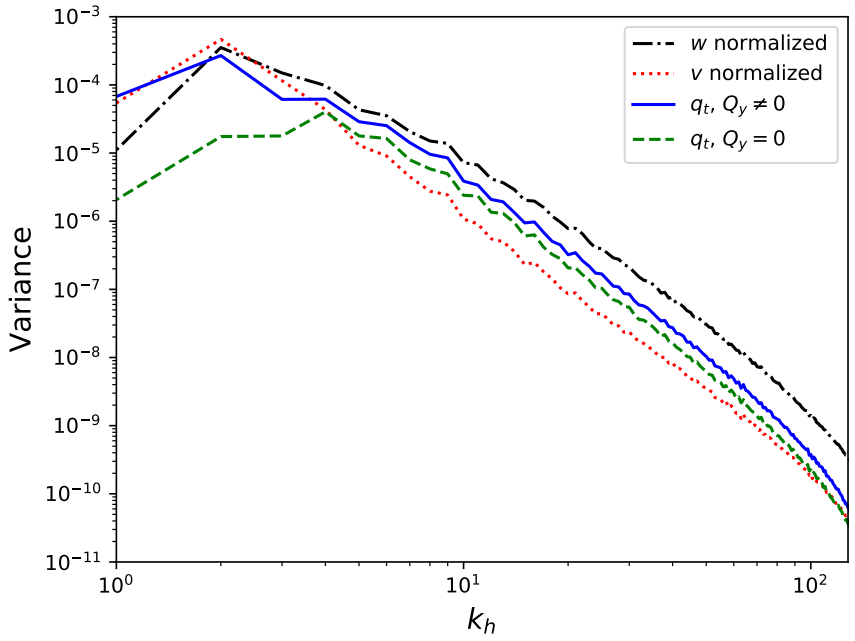

Figure 12.: Velocity and total water spectra for large $V_r = 10$. Baseline case with $Q_y = 0$ (zero Phillips background water): normalized v^2 (dash-dot); q_t^2 (dot). Case $|Q_y| = 1$ (non-zero meridional gradient of Phillips background water): normalized w^2 (solid); q_t^2 (dashed). For even larger values of V_r, the slope at large wavenumbers for both q_t spectra approach that of w. (Color online)

6. Discussion and conclusion

In summary, we have investigated the organization and structure of water in simulations of geostrophic turbulence. While this PQG model has the usual limitations from QG, along with those from having coarse, 2-level vertical resolution, it allows for understanding how

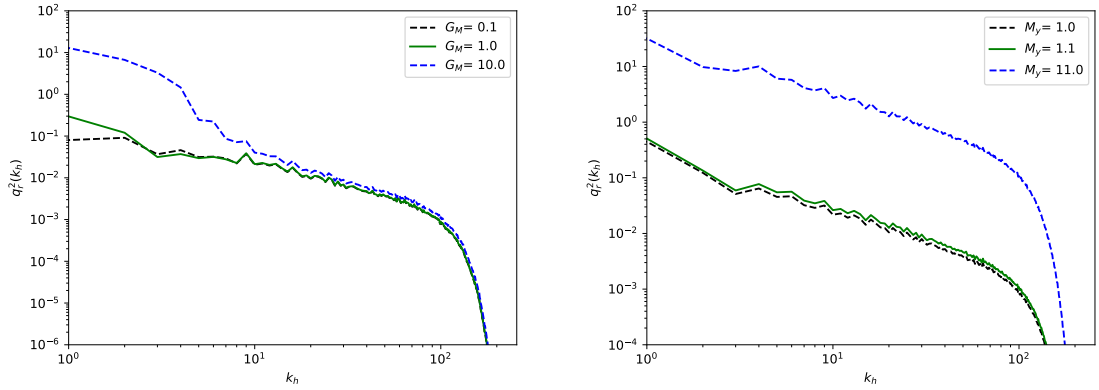

(a) $V_r = 0.001$

(b) $V_r = 0.001$

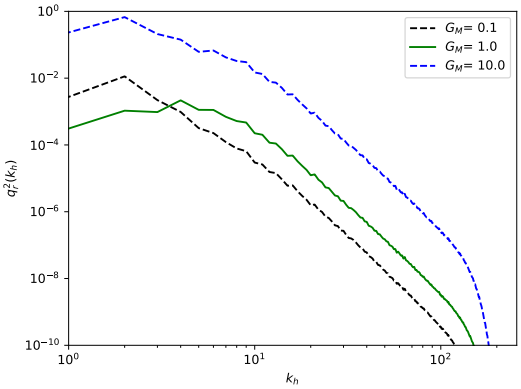

(c) $V_r = 1$

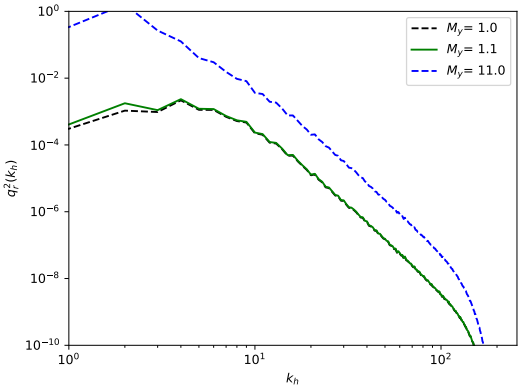

(d) $V_r = 1$

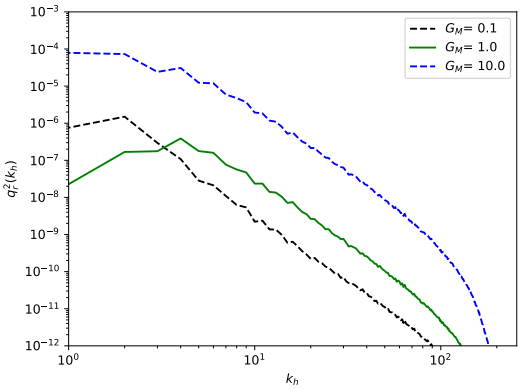

(e) $V_r = 100$

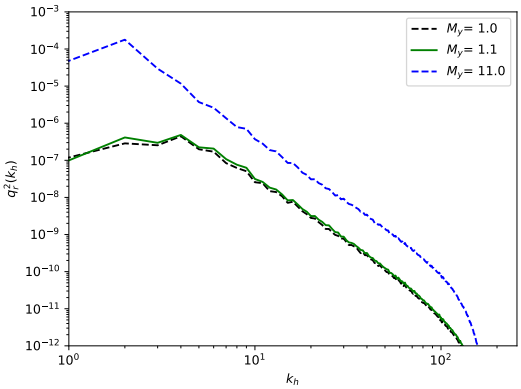

(f) $V_r = 100$

Figure 13.: Left column represents the change of the spectra based on changes in G_M and the right column represents that by changes in M_y. (Larger values of G_M, M_y correspond to curves higher up. The parameters G_M, M_y do not effect the behavior of the q_t spectra at high wave numbers. For low wave-numbers, we do see some difference, which can be explained from the combination of θ_e, M. (Note $M_y = (\cdot)$ should be considered as $M_y = (\cdot)\times$ base value. $M_y = 1.1$ corresponds with $Q_y = 0.1$.) (Color online)

precipitation influences statistics of water, in an idealized setting.

A main focus was to study the influence of precipitation on the variability of water. In the simple model setup here, the influence of precipitation can be controlled by varying the rainfall speed parameter, V_r, and it was seen that different behaviors can observed: small V_r leads to a prominent small-scale structure of water, while larger V_r essentially filters out the small scales. The model showed that for small V_r, a spectral exponent for q_t will be between -2 and -1, and for large V_r, the spectrum slope will approach that of w. Moreover, theoretical arguments provided explanations for these two asymptotic limits.

While it is natural to search for a clean fractional value for the spectral exponent, the results here are in line with the view that the spectral exponent in nature may not have a simple fractional value, as even with a PQG model which contains few parameters, by just adjusting the value of one, V_r, a continuum of possible spectral exponent values is obtained, ranging from around -1.4 to around -5. Moreover, with a presence of a meridional gradient of water, one can adjust the balance between the vertical and meridional to obtain a q_t which appears to be a combination of v and w in the limit of large V_r. In the case of comparable water gradients, there is a possibility that q_t will appear like v for a certain range and w for another, although this would require further investigation to understand in more detail.

Wave or mode decompositions provided a key perspective here for understanding water. In particular, it was shown that the water q_t could be written as a linear combination of two other variables: a passive tracer M and an active tracer θ_e, which correspond to a moist eigenmode and the vortical mode, respectively. In the case where the passive tracer is different from the active tracer, i.e. the small V_r regime, we saw that in our case, q_t behaved more as a passive tracer. In the case where the passive tracer (M) was forced to relax towards the active tracer (θ_e), the water q_t behaved as the difference between the passive tracer and active tracer, which in our case was w.

With the ability to provide a continuum of behavior for water while also providing asymptotic limits to the behavior, this study suggests that the two level PQG model provides a useful framework to study water in the atmosphere. In the future, it would be interesting to use the full version of the PQG equations including phase changes (Smith and Stechmann 2017), and/or to include the effects of a convective parameterization (e.g., as in Lapeyre and Held 2004), which would offer additional realism to the model, but likely at the expense of complicating theoretical analyses.

Acknowledgments

The authors thank two anonymous reviewers for helpful comments. Partial support for this research was provided by grants NSF AGS-1443325, NSF RTG DMS-1147523, NSF DMS-1907667, and the University of Wisconsin - Madison Office of the Vice Chancellor for Research and Graduate Education with funding from the Wisconsin Alumni Research Foundation.

References

Armi, L., Hydraulic control of zonal currents on a β-plane. *J. Fluid Mech.*, 1989, **201**, 357.

Babiano, A., Basdevant, C., Legras, B. and Sadourny, R., Vorticity and passive-scalar dynamics in two-dimensional turbulence. *J. Fluid Mech.*, 1987, **183**, 379–397.

Bannon, P.R., Linear development of quasi-geostrophic baroclinic disturbances with condensational heating. *J. Atmos. Sci.*, 1986, **43**, 2261–2274.

Booth, J.F., Polvani, L., O'Gorman, P.A. and Wang, S., Effective stability in a moist baroclinic wave. *Atmos. Sci. Lett.*, 2014, **16**, 56–62.

Brennan, M.J. and Lackmann, G.M., The influence of incipient latent heat release on the precipitation distribution of the 24-25 January 2000 US east coast cyclone. *Mon. Wea. Rev.*, 2005, **133**, 1913–1937.

Bretherton, C.S., Analytical solutions of Emanuel's model of precipitating convection. *J. Atmos. Sci.*, 1987, **44**, 3355–3355.

Charney, J.G., The dynamics of long waves in a baroclinic westerly current. *J. Meteor.*, 1947, **4**, 136–162.

Charney, J.G., On the scale of atmospheric motions. *Geofys. Publ. Oslo*, 1948, **17**, 1–17.

Charney, J.G., Geostrophic turbulence. *J. Atmos. Sci.*, 1971, **28**, 1087–1095.

Cho, J.Y.N., Newell, R.E. and Sachse, G.W., Anomalous scaling of mesoscale tropospheric humidity fluctuations. *Geophys. Res. Lett.*, 2000, **27**, 377–380.

Deng, Q., Smith, L.M. and Majda, A.J., Tropical cyclogenesis and vertical shear in a moist Boussinesq model. *J. Fluid Mech.*, 2012, **706**, 384–412.

Dolaptchiev, S.I. and Klein, R., A multiscale model for the planetary and synoptic motions in the atmosphere. *J. Atmos. Sci.*, 2013, **70**, 2963–2981.

Eady, E.T., Long waves and cyclone waves. *Tellus*, 1949, **1**, 33–52.

Edwards, T.K., Smith, L.S. and Stechmann, S.N., Atmospheric rivers and water fluxes in precipitating quasi-geostrophic turbulence. , 2019, p. submitted.

Emanuel, K.A., Some dynamical aspects of precipitating convection. *J. Atmos. Sci*, 1986, **43**, 2183–2198.

Emanuel, K.A., Fantini, M. and Thorpe, A.J., Baroclinic instability in an environment of small stability to slantwise moist convection. Part I: Two-dimensional models. *J. Atmos. Sci.*, 1987, **44**, 1559–1573.

Fischer, L., Kiemle, C. and Craig, G.C., Height-resolved variability of midlatitude tropospheric water vapor measured by an airborne lidar. *Geophys. Res. Lett.*, 2012, **39**, n/a–n/a.

Gall, R., The effects of released latent heat in growing baroclinic waves. *J. Atmos. Sci.*, 1976, **33**, 1686–1701.

Haidvogel, D.B. and Held, I.M., Homogeneous quasi-geostrophic turbulence driven by a uniform temperature gradient. *J. Atmos. Sci.*, 1980, **37**, 2644–2660.

Held, I.M. and O'Brien, E., Quasigeostrophic turbulence in a three-layer model: Effects of vertical structure in the mean shear. *J. Atmos. Sci.*, 1992, **49**, 1861–1870.

Hernandez-Duenas, G., Majda, A.J., Smith, L.M. and Stechmann, S.N., Minimal models for precipitating turbulent convection. *J. Fluid Mech.*, 2013, **717**, 576–611.

Houze, R., *Cloud dynamics*, 1993 (Academic Press, San Diego).

Kahn, B.H., Teixeira, J., Fetzer, E.J., Gettelman, A., Hristova-Veleva, S.M., Huang, X., Kochanski, A.K., Khler, M., Krueger, S.K., Wood, R. and Zhao, M., Temperature and water vapor variance scaling in global models: Comparisons to satellite and aircraft data. *J. Atmos. Sci.*, 2011, **68**, 2156–2168.

Kahn, B.H. and Teixeira, J., A global climatology of temperature and water vapor variance scaling from the atmospheric infrared sounder. *J. Climate*, 2009, **22**, 5558–5576.

Keeler, J.M., Jewett, B.F., Rauber, R.M., McFarquhar, G.M., Rasmussen, R.M., Xue, L., Liu, C. and Thompson, G., Dynamics of cloud-top generating cells in winter cyclones. Part I: Idealized simulations in the context of field observations. *J. Atmos. Sci.*, 2016a, **73**, 1507–1527.

Keeler, J.M., Jewett, B.F., Rauber, R.M., McFarquhar, G.M., Rasmussen, R.M., Xue, L., Liu, C. and Thompson, G., Dynamics of cloud-top generating cells in winter cyclones. Part II: Radiative and instability forcing. *J. Atmos. Sci.*, 2016b, **73**, 1529–1553.

Keeler, J.M., Rauber, R.M., Jewett, B.F., McFarquhar, G.M., Rasmussen, R.M., Xue, L., Liu, C. and Thompson, G., Dynamics of cloud-top generating cells in winter cyclones. Part III: Shear and convective organization. *J. Atmos. Sci.*, 2017, **74**, 2879–2897.

Klein, R. and Majda, A., Systematic multiscale models for deep convection on mesoscales. *Theor. Comp. Fluid Dyn.*, 2006, **20**, 525–551.

Kraichnan, R.H., Inertial ranges in two-dimensional turbulence. *Phys. Fluids*, 1967, **10**, 1417.

Kuo, H.l., Dynamic instability of two-dimensional nondivergent flow in a barotropic atmosphere. *J. Meteor.*, 1949, **6**, 105–122.

Lambaerts, J., Lapeyre, G. and Zeitlin, V., Moist versus dry baroclinic instability in a simplified two-Layer atmospheric model with condensation and latent heat release. *J. Atmos. Sci.*, 2012, **69**, 1405–1426.

Lapeyre, G. and Held, I.M., The role of moisture in the dynamics and energetics of turbulent baroclinic eddies. *J. Atmos. Sci.*, 2004, **61**, 1693–1710.

Larichev, V.D. and Held, I.M., Eddy amplitudes and fluxes in a homogeneous model of fully developed baroclinic instability. *J. Phys. Oceanogr.*, 1995, **25**, 2285–2297.

Majda, A.J., Xing, Y. and Mohammadian, M., Moist multi-scale models for the hurricane embryo. *J. Fluid Mech.*, 2010, **657**, 478–501.

Mak, M., On moist quasi-geostrophic baroclinic instability. *J. Atmos. Sci.*, 1982, **39**, 2028–2037.

Maltrud, M.E. and Vallis, G.K., Energy spectra and coherent structures in forced two-dimensional and beta-plane turbulence. *J. Fluid Mech.*, 1991, **228**, 321.

Mellado, J.P., Cloud-top entrainment in stratocumulus clouds. *Annu. Rev. Fluid Mech.*, 2017, **49**, 145–169.

Monteiro, J.M. and Sukhatme, J., Quasi-geostrophic dynamics in the presence of moisture gradients. *Q.J.R. Meteorol. Soc.*, 2015, **142**, 187–195.

Morrison, H. and Grabowski, W.W., Modeling supersaturation and subgrid-scale mixing with two-moment bulk warm microphysics. *J. Atmos. Sci.*, 2008, **65**, 792–812.

Nastrom, G.D., Jasperson, W.H. and Gage, K.S., Horizontal spectra of atmospheric tracers measured during the Global Atmospheric Sampling Program. *J. Geophys. Res.*, 1986, **91**, 13201.

Neelin, J.D. and Yu, J.Y., Modes of tropical variability under convective adjustment and the Madden–Julian oscillation. Part 1: Analytical theory. *J. Atmos. Sci.*, 1994, **51**, 1876–1894.

Pedlosky, J., *Geophysical Fluid Dynamics*, 1979 (Springer US).

Phillips, N.A., Energy transformations and meridional circulations associated with simple baroclinic waves in a two-level, quasi-geostrophic model. *Tellus*, 1954, **6**, 274–286.

Pressel, K.G. and Collins, W.D., First-order structure function analysis of statistical scale invariance in the AIRS-observed water vapor field. *J. Climate*, 2012, **25**, 5538–5555.

Qi, D. and Majda, A.J., Low-dimensional reduced-order models for statistical response and uncertainty quantification: Two-layer baroclinic turbulence. *J. Atmos. Sci.*, 2016, **73**, 4609–4639.

Rauber, R.M., Ellis, S.M., Vivekanandan, J., Stith, J., Lee, W.C., McFarquhar, G.M., Jewett, B.F. and Janiszeski, A., Finescale structure of a snowstorm over the northeastern United States: A first look at high-resolution HIAPER cloud radar observations. *Bull. Amer. Meteor. Soc.*, 2017, **98**, 253–269.

Read, P.L., Atmospheric and Oceanic Fluid Dynamics: Fundamentals and Large-Scale Circulation Geoffrey K. Vallis. ISBN 0-5218-4969-1. Cambridge University Press 2007. 770 pages.. *Q.J.R. Meteorol. Soc.*, 2007, **133**, 2145–2146.

Rhines, P.B., Geostrophic turbulence. *Annu. Rev. Fluid Mech.*, 1979, **11**, 401–441.

Rogers, R. and Yau, M., *A short course in cloud physics*, 1989 (Butterworth–Heinemann, Burlington).

Salmon, R., Baroclinic instability and geostrophic turbulence. *Geophysical & Astrophysical Fluid Dynamics*, 1980, **15**, 167–211.

Salmon, R., *Lectures on geophysical fluid dynamics*, 1998 (Oxford University Press).

Schemann, V., Stevens, B., Grtzun, V. and Quaas, J., Scale dependency of total water variance and its implication for cloud parameterizations. *J. Atmos. Sci.*, 2013, **70**, 3615–3630.

Seitter, K.L. and Kuo, H.L., The dynamical structure of squall-line type thunderstorms.. *J. Atmos. Sci.*, 1983, **40**, 2831–2854.

Smith, K.S. and Vallis, G.K., The scales and equilibration of midocean eddies: Freely evolving flow. *J. Phys. Oceanogr.*, 2001, **31**, 554–571.

Smith, L.M. and Stechmann, S.N., Precipitating quasi-geostrophic equations and potential vorticity inversion with phase changes. *J. Atmos. Sci.*, 2017.

Spyksma, K. and Bartello, P., Small-scale moist turbulence in numerically generated convective clouds. *J. Atmos. Sci.*, 2008, **65**, 1967–1978.

Sukhatme, J., Majda, A.J. and Smith, L.M., Two-dimensional moist stratified turbulence and the emergence of vertically sheared horizontal flows. *Phys. Fluids*, 2012, **24**, 036602.

Thorpe, A.J. and Emanuel, K.A., Frontogenesis in the presence of small stability to slantwise convection. *J. Atmos. Sci.*, 1985, **42**, 1809–1824.

Wetzel, A.N., Smith, L.M. and Stechmann, S.N., Moisture transport due to baroclinic waves: Linear analysis of precipitating quasi-geostrophic dynamics. *Math. Clim. Weather Forecast.*, 2017, **3**, 28–50.

Wetzel, A.N., Smith, L.M. and Stechmann, S.N., Discontinuous fronts as exact solutions to precipitating quasi-geostrophic equations. *SIAM J. Appl. Math.*, 2019a, **79**, 1341–1366.

Wetzel, A.N., Smith, L.M., Stechmann, S.N. and Martin, J.E., Balanced and unbalanced components of moist atmospheric flows with phase changes. *Chin. Ann. Math. B*, 2019b, p. in press.

Whitaker, J.S. and Davis, C.A., Cyclogenesis in a saturated environment. *J. Atmos. Sci.*, 1994, **51**, 889–908.

Zhang, F., Bei, N., Rotunno, R., Snyder, C. and Epifanio, C.C., Mesoscale predictability of moist baroclinic waves: Convection-permitting experiments and multistage error growth dynamics. *J. Atmos. Sci.*, 2007, **64**, 3579–3594.

Appendix A: Details on $\tilde{q}_t, \tilde{q}_r$

The saturation water vapor takes the value of its background state, so that $q_{vs}^{tot} = \tilde{q}_{vs}$. Taken together, since $\tilde{q}_t = \tilde{q}_v + \tilde{q}_r = q_{vs}^{tot} + \tilde{q}_r$ and the water vapor is always at its saturation value, the anomalies of total water are equal to the anomalies of rain water: $q_t = q_r$. The saturation water vapor $q_{vs}^{tot}(z)$ is taken to be a function of z, since $q_{vs}^{tot}(T^{tot}, p^{tot}) \approx q_{vs}^{tot}(\tilde{T}(z), \tilde{p}(z))$ in this Boussinesq setup where the anomalies T and p are small compared with the background states $\tilde{T}(z)$ and $\tilde{p}(z)$ (e.g., Hernandez-Duenas *et al.* 2013). For an environment that remains saturated for all time, the total mixing ratio of water vapor q_v^{tot} is always equal to a prescribed saturation function of altitude $q_{vs}^{tot}(z)$, such that $q_v^{tot} = q_{vs}^{tot}$. Furthermore, the mixing ratio of total water q_t^{tot} is always above saturation, with $q_r^{tot} = q_t^{tot} - q_{vs}^{tot} > 0$. The latter inequality, in turn, implies that the background rain $\tilde{q}_r$ must be sufficiently large to allow for negative anomalies in our simulations (see section 3).

Appendix B: Computation of w

The values for w is obtained by solving the ω equation,

$$-\left[\frac{2}{\Delta z}-\nabla_h^2\left(\frac{L_{ds}}{L}\right)^2\Delta z\right]w = \Big[[(v_2-v_1)\beta+\left[J(\psi_2,\nabla_h^2\psi_2)-J(\psi_1,\nabla_h^2\psi_1)\right] + \nabla_h^2(v_2u_1-u_2v_1)\ +\ kappa_M\nabla^2\psi_1+2U\nabla_h^2\partial_x\left(\psi_2+\psi_1\right)\Big], \tag{B.1}$$

where $J(a,b)$ represents the determinant of the jacobian. The horizontal derivatives are computed spectrally in Fourier space.

Appendix C: Baroclinic instability of the linearized PQG equations in a saturated environment

In the numerical simulations, the initial conditions are a band of linearly unstable eigenmodes. In what follows, these eigenmodes are presented for the PQG equations. The PGQ eigenmodes are similar to the dry QG eigenmodes, but they differ because of the additional moist variable M, as explained below.

The effect of water on the linear stability of the two-level PQG equations can be studied by solving the 'Phillips problem' (Phillips 1954), which is perhaps the simplest framework to study baroclinic instability on a β-plane. Related formulations of the linear stability problem for the dry QG equations may be found in (Salmon 1980, Read 2007, Pedlosky 1979).

From (8) written in terms of the streamfunction ψ and M, one can see that (8a,b) form a closed subsystem for ψ which is mathematically equivalent to the dry Phillips formulation. There is only a one-way coupling with (8c), such that ψ influences the dynamics of M but not the other way around. As will be verified below, the presence of moisture does not introduce new instabilities, but only changes the range of unstable wavelengths and growth rates. The effect of moisture on the growth rate of unstable modes has been examined in previous studies, such as Emanuel *et al.* (1987), Lapeyre and Held (2004). The linear instability analysis of the continuously stratified PQG equations without the β-effect (the so-called Eady problem Eady 1949, Pedlosky 1979) has been studied in Wetzel *et al.* (2017). Moist baroclinic instability has also been studied in other contexts (such as in Gall 1976, Thorpe and Emanuel 1985, Whitaker and Davis 1994, Zhang *et al.* 2007, Booth *et al.* 2014). It was observed in Wetzel *et al.* (2017) that with the continuous PQG in a saturated regime, the ratio between the moist and dry maximum growth rates were comparable to that found in Gall (1976). However, the wavenumber of the maxmimum growth rate was unchanged in Gall (1976) even with moisture, whereas for Wetzel *et al.* (2017), the wavenumber increased.

To impose a zonal flow with vertical shear, together with a meridional temperature gradient, the Phillips background streamfunction is chosen at levels $j=1,2$ to be $\psi_{j,bg}=U_jy$ with $U_j=(-1)^jU$ and U constant (Haidvogel and Held 1980, Lapeyre and Held 2004). The resulting expressions for θ_e and PV are, respectively, $\theta_{e,bg}=\Theta y=-\left(L/L_{ds}\right)\left(1/\Delta z\right)\left(2Uy\right)$ and $PV_{j,bg}=\left(-1\right)^j\left(1/\Delta z\right)^2\left(L/L_{ds}\right)^2\left(2Uy\right)$. For analysis of the saturated environment, we also impose a background water profile $q_{t,bg}=Q_yy$ with Q_y constant. Thus both temperature and water decrease linearly from south to north. From here on, all variables are decomposed into Boussinesq and Phillips background state and anomalies, in which case the equations (8)

may be written as

$$\frac{\mathrm{D}_1 PV_1}{\mathrm{D}t} - U\partial_x PV_1 + v_1 \partial_y PV_{1,bg} + \beta v_1 \;= 0\,, \tag{C.1a}$$

$$\frac{\mathrm{D}_2 PV_2}{\mathrm{D}t} + U\partial_x PV_2 + v_2 \partial_y PV_{2,bg} + \beta v_2 \;= 0\,, \tag{C.1b}$$

$$\frac{\mathrm{D}_m M}{\mathrm{D}t} + v_m \partial_y M_{bg} \;= -\;\frac{V_r}{\Delta z}\,(M - G_M \theta_e)\,, \tag{C.1c}$$

where $M_{bg} = q_{t,bg} + G_M \theta_{e,bg} = (Q_y + G_M \Theta) y$.

The linearized version of (C.1) has constant coefficients U, β, Q_y, G_M, V_r, and thus one may look for exponential solutions $\psi_j = \mathrm{Re}\{\hat{\psi}_j e^{\mathrm{i}(kx+ly-\omega t)}\}$ and $M = \mathrm{Re}\{\hat{M} e^{\mathrm{i}(kx+ly-\omega t)}\}$, leading to the possible values of ω:

$$\omega^{\pm} \;= -\,\frac{k}{k_h^2 + k_{ds}^2}\left\{\beta\left(1 + \frac{k_{ds}^2}{2k_h^2}\right) \mp \frac{k_{ds}^2}{2k_h^2}\left[\beta^2 + \frac{4U^2 k_h^4 (k_h^4 - k_{ds}^4)}{k_{ds}^4}\right]^{1/2}\right\}, \tag{C.2a}$$

$$\omega^{r} \;= -\,\mathrm{i}\frac{V_r}{\Delta z}\,, \tag{C.2b}$$

with $k_h = \sqrt{k^2 + l^2}$ and $k_{ds}^2 = 8L^2/L_{ds}^2$.

To simplify the notation, $\hat{\psi}_1, \hat{\psi}_2$ are used to represent the eigenmodes found from the solution of the two level dry QG linearized instability problem. (For more details, see Read 2007, Pedlosky 1979).

The eigenmode associated with $\omega^{\pm}$ is given by

$$\begin{pmatrix} \hat{\psi}_1 \\ \hat{\psi}_2 \\ -\dfrac{1}{-\mathrm{i}\omega^{\pm} + V_r/\Delta z}\left[\dfrac{V_r}{\Delta z}\left(G_M \dfrac{L}{L_{ds}} \dfrac{\hat{\psi}_2 - \hat{\psi}_1}{\Delta z}\right) - \mathrm{i}k \dfrac{\hat{\psi}_1 + \hat{\psi}_2}{2} M_{bg}\right] \end{pmatrix} \tag{C.3}$$

and that associated with ω^r is given by

$$\big(\,0\,,\,0\,,\,1\,\big)^{\mathrm{T}}\,. \tag{C.4}$$

The initial conditions for $\hat{\psi}_1, \hat{\psi}_2$ are obtained from a band of these eigenmodes, with uniformly random phase, as in the dry case. For the initial condition of $\hat{M}$, the linear combination of the $M-$component of $\omega^{\pm} + \alpha\beta\omega^r$ is used, with α being the amplitude of the wave from ω^{pm} and β being a random number chosen from a normal distribution.